Chinese Journal of
POLYMER SCIENCE

RESEARCH ARTICLE

https://doi.org/10.1007/s10118-026-3659-9
Chinese J. Polym. Sci. **2026**, *44*, 2659–2669

Micro-sized Silicon Carbonitride Prepared by Radical Polymerization as a High-performance Anode Material for Lithium-ion Batteries

Xin Xia, Zhen-Peng Zhang, De-Shuo Wang, Yi-Han Li, Jing-Jiang Sun, Jian-Jiang He, Qing-Fu Wang*, and Wei Zhao*

Key Laboratory of Rubber-plastics, Ministry of Education, School of Polymer Science and Engineering, Qingdao University of Science and Technology, Qingdao 266042, China

Electronic Supplementary Information

Abstract To address the critical issue of volume expansion in silicon-based anode materials and enhance battery performance, a novel method for synthesizing microsized silicon carbonitride (SiCNO) ceramic particles was presented as a high-performance anode material for lithium-ion batteries. SiCNO ceramic microspheres were prepared *via* high-temperature pyrolysis of organopolysilazane microspheres (OPSZ MPs), which were synthesized *via* free radical polymerization of silazane oligomers initiated by azobisisobutyronitrile (AIBN). The SiCNO microspheres, serve as the active materials in lithium-ion batteries anode, demonstrated excellent electrochemical performance with an initial discharge-specific capacity of 1663.3 mAh·g^{-1} and 622.9 mAh·g^{-1} after 400 cycles at 1 A·g^{-1}. These microspheres exhibited superior structural stability during the lithiation and delithiation processes, with a volume expansion of 25.46% during cycling. The enhanced performance can be attributed to their regular spherical structures and larger specific surface area, which improve the ion/electron transport and stress distribution. This study highlights the potential of synthesizing and regulating the morphology of SiCNO particles to improve the performance of anode materials for lithium-ion batteries, providing a balance between high electrochemical activity and structural stability.

Keywords Lithium-ion batteries; Silicon/Carbon composite anode; Micro-sized particles; Polysilazane

Citation: Xia, X.; Zhang, Z. P.; Wang, D. S.; Li, Y. H.; Sun, J. J.; He, J. J.; Wang, Q. F.; Zhao, W. Micro-sized silicon carbonitride prepared by radical polymerization as a high-performance anode material for lithium-ion batteries. *Chinese J. Polym. Sci.* **2026**, *44*, 2659–2669.

INTRODUCTION

The design and synthesis of advanced anode materials are crucial for addressing the limitations of conventional lithium-ion batteries. Silicon-based anodes are highly promising because of their exceptional theoretical capacity (about 4200 mAh·g^{-1}).[1] However, their practical application is hindered by significant volume expansion (about 300%) during lithiation,[2,3] which leads to electrode degradation and rapid capacity fading. Polymer-derived ceramics (PDCs), particularly those derived from organosilicon precursors with Si—C or Si—N frameworks, offer a promising solution owing to their adjustable molecular structures and stability after pyrolysis.

Recent progress in preceramic polymer chemistry, such as using polysiloxanes, polycarbosilanes, and polysilazanes, has facilitated the development of SiCO and SiCN ceramic materials with enhanced lithium storage properties[4]. Among these, polysilazanes, featuring a Si—N backbone, are especially advantageous for synthesizing Si—C—N ceramics. Nevertheless, the fabrication of uniform discrete PDC particles (*e.g.*, microspheres) remains a challenge. To address this, free-radical polymerization has been employed to produce monodisperse polymer microspheres with excellent dispersibility. Key parameters, such as monomer concentration, initiator ratio, temperature, and stirring rate, critically influence the microsphere size and morphology.[5,6] For instance, Zhang *et al.*[7] used an emulsion method with an inert fluorinated solvent (FC-70) and UV-initiated radical polymerization to synthesize vinylsilazane-derived nanoparticles. When combined with graphene oxide, these ceramic SiCNO nanoparticles demonstrated that higher active material loading leads to better lithium storage, underscoring the importance of controlled synthesis in optimizing the electrochemical performance.

In this study, monodisperse organic polysilazane microspheres (OPSZ MPs) were synthesized by homogeneous free radical polymerization using azodiisobutyronitrile (AIBN) as the initiator, enabling precise particle size control and efficient solvent processing. Subsequent pyrolysis yielded SiCNO ceramic microspheres (SiCNO MPs) with a uniform morphology and superior dispersibility. Radical polymerization was successfully introduced into the morphology synthesis of polymer-derived ceramics (PDC), which realized the "bridge" construction from organic polymers to inorganic ceramics.

* Corresponding authors, E-mail: wangqf@qust.edu.cn (Q.F.W.)
E-mail: zwqust@qust.edu.cn (W.Z.)
Received January 12, 2026; Accepted March 11, 2026; Published online June 9, 2026

Compared to their bulk-polymerized counterparts (SiCNO HT), the SiCNO MPs were micron-sized solid spheres that effectively resisted internal stresses during lithium insertion/deintercalation processes, while simultaneously suppressing particle pulverization. Micron spheres exhibited a higher tap density, improved packing behavior, mitigated parasitic side reactions, and enhanced volumetric capacity. As Li-ion battery anodes, the SiCNO MPs delivered outstanding cycling stability, retaining a reversible capacity of 622.9 mAh·g^{-1} after 400 cycles at 1 A·g^{-1}. These findings highlight the pivotal role of synthesis engineering in tailoring the microstructure and electrochemical properties of PDC-based materials for next-generation energy-storage applications.

EXPERIMENTAL

Materials

Dichloromethylsilane (98%), dichloromethylvinylsilane (97%), aminopropyltriethoxysilane (99%) (all purchased from Sigma-Aldrich, Shanghai), *n*-hexane (Sinopharm Chemical Reagent, Shanghai, China), azodiisobutyronitrile (AIBN), anhydrous acetonitrile (Energy Chemical, Shanghai), and anhydrous ethanol (Sinopharm Chemical Reagent, Shanghai, China) were used.

Synthesis of Organopolysilazane Oligomer OPSZ 1001

To a 2 L three-necked round-bottom flask equipped with a stirrer, thermometer, and dry ice/isopropanol condenser, 600 mL of hexane was added. Then, methyltrichlorosilane (0.24 mol, 27.6 g) and methylvinyldichlorosilane (0.06 mol, 8.4 g) were sequentially added to the reactor, followed by the addition of 3-aminopropyltriethoxysilane (0.3 mol, 66.42 g). The mixture was cooled to approximately 20 °C in an ice bath and stirred for 2 h. Ammonia vapor was slowly introduced into the reactor and the temperature was maintained at approximately 20 °C for 2 h. Upon completion of the ammonolysis reaction, the ammonium chloride precipitate was removed *via* filtration. Subsequently, the precipitate was extracted thrice with *n*-hexane (100 mL). Finally, excess ammonia and solvent were removed by evaporation under reduced pressure at 40 °C, affording a liquid organopolysilazane oligomer (OPSZ 1001).

Preparation of OPSZ MPs

The organopolysilane oligomer (OPSZ 1001) was dissolved in 10 mL of anhydrous acetonitrile, and then the initiator AIBN was added to dissolve rapidly. Oxygen was removed from the reaction system through freeze-pump-thaw cycles and the reaction was carried out at 60 °C under argon protection. After 8 h, the reaction solution was removed and centrifuged at 8000 r·min^{-1} for 10 min, and the excess solvent and unreacted monomers were removed. The precipitate was redispersed in anhydrous ethanol and ultrasonicated for 10 min. Centrifugation and rinsing were repeated three times, and the OPSZ MPs were vacuum dried at 80 °C for 12 h.

Preparation of SiCNO MPs and SiCNO HT

SiCNO MPs were prepared by pyrolyzing OPSZ MPs under a nitrogen atmosphere at a heating rate of 10 °C·min^{-1} up to 1000 °C, followed by a dwell time of 3 h at this temperature. SiCNO ceramic powder (denoted as SiCNO HT) was obtained by pyrolysis of a high-temperature-cured organopolysilazane (OPSZ HT). This process involved first curing OPSZ 1001 at 80 °C for 24 h. Subsequently, the cured product was ground into a powder using an agate mortar and subjected to ball milling at 300 r·min^{-1} for 6 h to yield OPSZ HT. Finally, SiCNO HT was obtained by pyrolyzing OPSZ HT at 1000 °C under a nitrogen atmosphere, employing a heating rate of 10 °C·min^{-1} and a dwell time of 3 h.

Structural Characterization

The structure of OPSZ1001 was analyzed by Fourier transform infrared spectroscopy (FTIR) using a Bruker VERTEX70 instrument. The morphologies of the OPSZ and SiCNO MPs were characterized by transmission electron microscopy (TEM, JEM2100) and scanning electron microscopy (SEM, JSM7500F), and the samples were centrifuged using a benchtop high-speed centrifuge (TG16-WS). X-ray diffraction (XRD) patterns were recorded using a Rigaku D/MAX/2500PC X-ray diffractometer. The surface chemical states of the elements in the ceramic composites were determined using X-ray photoelectron spectroscopy (XPS, Thermo Fisher, ESCALAB XI+).

Half-cell Assemble and Electrochemical Studies

Ceramic SiCNO MPs and SiCNO HT prepared by pyrolysis of OPSZ MPs and OPSZ HT were used as the active anode materials for lithium-ion batteries. Carboxymethyl cellulose (CMC) and styrene-butadiene latex (SBR) were used as binders, and conductive carbon black super p was used as the conductive agent, which was uniformly dispersed in H_2O to form a homogeneous slurry according to the formula SiNCO:super p:CMC:SBR= 6:2:1.2:0.8. Then, the slurry was scraped and coated on top of a copper foil with a thickness of 150 μm. After standing for 2 h, the coating was then dried in a vacuum oven at 80 °C for 12 h. The SiCNO ceramic working electrode and lithium metal sheet (diameter 16 mm, thickness 0.6 mm) were assembled into a 2032 button battery, with the lithium metal sheet serving as the negative counter electrode. All operations were performed in an argon-filled glove box (H_2O and O_2 content < 0.01 cm^3/m^3). The electrolyte was a 1 mol·L^{-1} $LiPF_6$ solution in a mixed solution of dimethyl carbonate and ethylene carbonate (volume ratio 1:1). The electrodes were separated using a Celgard 2500 separator (thickness, 25 μm; diameter, 18 mm). The electrochemical performance of the battery was tested on the Land 3002A battery testing system (Wuhan Dadi Electronics Co., Ltd., China Wuhan) under room temperature and constant current density conditions, with a cutoff voltage of 0.01–2.0 V (versus Li/Li$^+$). All the specific capacities were calculated based on the mass of the SiCNO ceramic.

RESULTS AND DISCUSSION

In this study, polysilazane microspheres (OPSZ MPs) were synthesized *via* free-radical polymerization in a homogeneous solution of vinyl dichlorosilane and dimethyldichlorosilane co-ammonolysis products using AIBN as the initiator. Acetonitrile was selected as the solvent because of its good solubility, chemical inertness, and compatibility with the free-radical polymerization system, which is helpful for achieving uniform monomer dissolution and controllable microsphere formation. By systematically optimizing the reaction parameters, including the time, temperature, initiator concentration, and monomer ratio, we developed a controllable method to produce highly uniform and well-dispersed microspheres. The resulting OPSZ MPs ex-

https://doi.org/10.1007/s10118-026-3659-9

hibited excellent potential as preceramic precursors for advanced ceramics and energy storage applications. Electrochemical evaluations in half-cell configurations revealed their promising performance as anode materials for lithium-ion batteries, offering high energy density and exceptional cycling stability. These properties stem from the uniform morphology of the microspheres and their tailored chemical composition, which mitigates structural degradation during cycling. This study highlights the critical role of precise synthesis control in the development of high-performance polymer-derived ceramic materials for next-generation battery technologies.

Synthesis and Characterization of Organopolysilazane Oligomers (OPSZ 1001)

OPSZ 1001 was synthesized *via* ammonolysis of methylvinyldichlorosilane, methyldichlorosilane, and aminopropyltriethoxysilane. The chemical structure of the obtained oligomer was characterized by proton nuclear magnetic resonance (^{1}H-NMR) and Fourier transform infrared (FTIR) spectroscopy. ^{1}H-NMR spectroscopy (Fig. S1 in the electronic supplementary informaiton, ESI) showed the presence of —Si—CH=CH_2 (6.23–5.63 ppm), —Si—H (4.86–4.31 ppm), and —Si—CH_3 (0.34–0.07 ppm) groups, which was in agreement with the FTIR spectroscopy results. FTIR provided complementary structural information, as shown in Fig. S2 (in ESI). The following characteristic absorption peaks were observed in the spectrum: the C—H stretching vibrations of the vinylsiloxane group (—Si—CH=CH_2) appeared at 3053 and 2974 cm^{-1}, and the C=C stretching vibration peak was located at 1598 cm^{-1}. A prominent absorption peak corresponding to the —Si—H bond is observed at 2140 cm^{-1}. The absorption peaks assigned to the —Si—NH—Si structure included the N—H stretching vibration at 3394 cm^{-1} and the Si—N vibration at 953 cm^{-1}. Additionally, the —Si—CH_3 group exhibited a characteristic absorption peak at 1251 cm^{-1}, accompanied by C—H stretching vibrations at 2931 and 2885 cm^{-1}. The concordance of these spectroscopic analyses confirmed the successful synthesis and structural integrity of organopolysilazane oligomers.

Preparation of Organopolysilazane Microspheres (OPSZ MPs) by Free Radical Polymerization and Particle Size Regulation

The OPSZ MPs were prepared *via* free-radical polymerization. The preparation process is illustrated in Fig. 1. The morphology, particle size, and particle size distribution of the OPSZ MPs can be effectively controlled by adjusting the concentration, reaction temperature, and initiator dosage of OPSZ 1001 during polymerization.

First, under certain conditions (OPSZ 1001 concentration: 0.05 mol·L^{-1}, initiator AIBN: 1%, reaction temperature: 50 °C), the effects of different reaction times on the size and particle size distribution of nanoparticles were investigated. As shown in Fig. S3 (in ESI), the particle size of the OPSZ MPs increased with increasing reaction time, the microspheres became irregular, and the particle size distribution was uneven after 12 h. At 8 h, the particle size distribution was the most uniform, with regular spherical shapes, and an average particle size of approximately 1.3 μm. Therefore, an optimal reaction time of 8 h was selected for the follow-up study.

To further optimize the synthesis parameters, the effects of monomer concentration, initiator dosage, and reaction temperature on the particle morphology and size distribution were systematically studied, as summarized in Table 1.

The reaction temperature played a critical role in determining the particle morphology and size distribution. As evidenced by SEM analysis (Fig. S4 in ESI), microspheres synthesized at 55–60 °C displayed optimal uniformity in both size and shape. At lower temperatures, the reduced polymerization rate resulted in irregular particle formation, whereas elevated temperature (>60 °C) promoted excessive AIBN decomposition. This leads to an uncontrolled increase in the free radical concentration, causing rapid polymerization kinetics and, consequently, broader particle size distributions.[8] Systematic evaluation of these thermal effects established 55–60 °C as the optimal temperature range for producing monodisperse microspheres with well-defined morphologies.

Subsequently, the effect of initiator concentration on the morphology and size distribution of the OPSZ MPs was systematically investigated. As shown in Table 1 and Fig. S5 (in ESI), the diameter of the OPSZ MPs gradually increased with increasing initiator content, resulting in inhomogeneous particles. This phenomenon can be attributed to the increased radical formation at elevated initiator levels, which promotes excessive grafting of vinylsilane monomers onto particle surfaces and consequently results in uncontrolled particle growth. Optimal uniformity was achieved at an AIBN:OPSZ 1001 molar ratio of 1:100 (1% initiator), yielding monodisperse microspheres with a diameter of 1.6 μm (Fig. S5f in ESI).

Finally, the influence of the OPSZ 1001 concentration was assessed. SEM images in Fig. S6 (in ESI) revealed that an OPSZ 1001 concentration of 0.01 mol·L^{-1} produced microspheres with optimal size uniformity. Increasing the monomer concentration resulted in larger particle diameters and broader

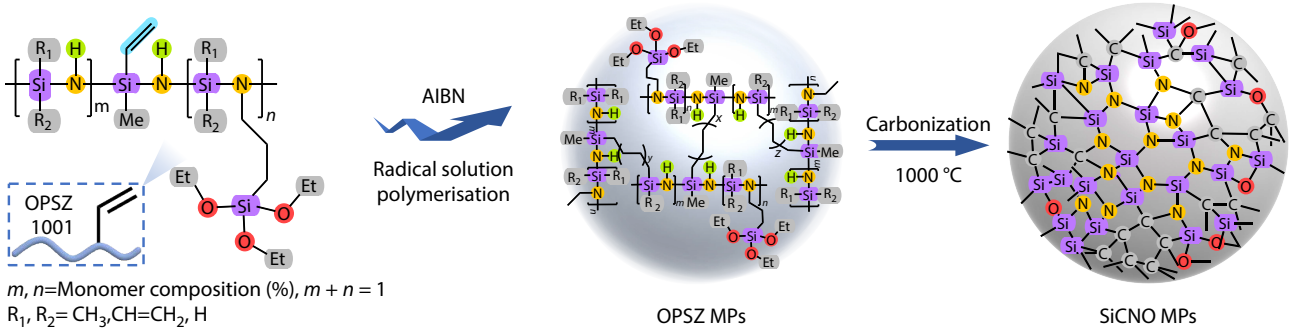

Fig. 1 Schematic representation of SiCNO ceramic microparticles prepared using free radical polymerization.

https://doi.org/10.1007/s10118-026-3659-9

Table 1 Summary of OPSZ MPs synthesized by free radical polymerization under different conditions.

Entry	OPSZ 1001 (mol·L^{-1})	AIBN content (%)	Temperature (°C)
1	0.05	1	45
2	0.05	1	50
3	0.05	1	55
4	0.05	1	60
5	0.05	1	65
6	0.05	0.5	60
7	0.05	1	60
8	0.05	2	60
9	0.05	4	60
10	0.05	8	60
11	0.01	1	60
12	0.05	1	60
13	0.1	1	60
14	0.15	1	60
15	0.2	1	60

size distributions accompanied by observable polymer agglomeration. This concentration-dependent behavior stems from enhanced polymerization kinetics at elevated monomer levels, which promotes (1) excessive radical generation and (2) non-uniform particle growth rates.

Characterisation of Morphology, Structure and Composition of Organopolysilazane Microspheres (OPSZ MPs)

The silazane oligomers (OPSZ 1001) were polymerized by free radicals to form organosilazane networks. In the spectral band of OPSZ 1001 (Fig. 2a), absorption peaks attributed to —Si—H can be observed at 2140 cm^{-1}. The bands associated with Si—NH—Si included N—H stretching at 3394 cm^{-1} and Si—N vibrations at 953 cm^{-1}. The energy bands for vinyl (Si—CH=CH$_2$) were C—H stretching vibrations at 2974 and 3053 cm^{-1}, respectively, and a C=C stretching vibration was observed at 1598 cm^{-1}. The characteristic band of the Si—CH$_3$ group was located at 1251 cm^{-1}. The weakening of the —Si—H and N—H peaks during the free radical polymerization of the silazane oligomers is due to dehydrogenation between the —Si—H and —N—H groups or the addition of hydrosilanes to the C=C bond.[9,10] The SiCNO ceramic MPs were produced by pyrolysis of OPSZ MPs at 1000 °C. The transformation from polymer to ceramic was confirmed by FTIR spectra of the microspheres. During pyrolysis at 1000 °C under nitrogen, C—Si and Si—O bonds exhibited greater stability compared to C—H bonds. In polysilazane, the peaks assigned to the —Si—CH$_3$ (about 1259 cm^{-1}) and —CH$_2$— (about 2972 cm^{-1}) groups disappeared, whereas peaks attributed to Si—O (about 1076 cm^{-1}) and —Si—C— (about 821 cm^{-1}) bonds emerged after pyrolysis.[11,12] Simultaneously, in the XRD spectra of Fig. 2(b), there are broad diffraction peaks at about 23° and about 43°, indicating that the SiCNO microspheres are amorphous after decomposition at 1000 °C. As shown in Fig. 2(c), the Raman spectra of the SiCNO sample show typical peaks at 1358 and 1598 cm^{-1}, indicating that free carbon was also formed during the carbonization of SiCNO.[13]

There was a significant difference between the OPSZ obtained by bulk polymerization and free-radical polymerization. OPSZ HT shows an uneven block structure (Fig. 2d), while OPSZ MPs show a uniform spherical appearance; after the ceramic process, they still maintain a good spherical morphology and dispersion. Scanning electron microscopy (SEM) and the corresponding elemental mapping spectrogram (EDS) plots show the distribution of Si, C, N, and O in the OPSZ MPs (Fig. 2g) and SiCNO MPs (Fig. 2h), indicating that Si, C, N, and O are uniformly distributed on the surface of the spherical particles. The distribution of C in the elemental mapping images of the ceramicist particles was slightly different from that of the other three elements, which may be due to the generation of free carbon during the carbonization process.

The X-ray photoelectron spectroscopy (XPS) analysis of the Si 2p peak demonstrates a shift from the binding energy peak center of OPSZ MPs at 102.6 eV to 101.7 eV in SiCNO, indicating a change in the silicon valence state after Si—O bond fracture during pyrolysis. Specifically, the silicon band (Si 2p) of OPSZ MPs was deconvoluted into two peaks at 102.2 and 101.4 eV, which correspond to Si—O and Si—C, respectively. (Fig. S7a in ESI). This decrease in the SiO$_2$ phase indicated that the Si—O bond was broken during the pyrolysis process. The oxygen bands (O 1s) of Si—O and SiO$_2$ peak at 531.2 and 531.6 eV, respectively, with the change in O 1s peak intensity confirming Si—O bond fracture during pyrolysis (Fig. S7b in ESI). In the C 1s spectrum, SiCNO MPs exhibited peaks at 283.4 and 284.8 eV, which correspond to the C—Si bond and C—C/C=C bonds, respectively. Notably, the C=C bonds present in the OPSZ MPs were completely consumed during the polymerization process. As shown in Fig. S7(c) (in ESI), the increase in the C—Si peak intensity following pyrolysis suggests a reaction between carbon and silicon, resulting in the formation of additional C—Si phases at 1000 °C. This observation was also supported by the Si 2p band. Additionally, C—O/C—N component at 286.8 eV confirms the nitrogen doping.[14,15] The N1s peak at 399.4 eV shown in Fig. S7(d) (in ESI) indicates successful nitrogen doping, with contributions from N—Si and N—C molecules observed at 398.8 and 400.4 eV, respectively.

Electrochemical Performances as Anode for Lithium-ion Batteries

The SiCNO MPs and SiCNO HT were studied using cyclic voltammetry (CV) to examine their lithium-ion insertion/extraction behavior. Fig. 3 shows the CV curve of the SiCNO electrode over the first five cycles at a scan rate of 0.1 mV·s^{-1}. The SiCNO MPs electrode exhibited a broad reduction peak at approximately 0.76 V, which disappeared in subsequent cycles, indicating the formation of a stable SEI film on the material surface.[16] In addition, the reduction peak observed between 1–1.5 V was associated with irreversible reactions involving lithium silicate (Li_4SiO_4, $Li_2Si_2O_5$) and Li_2O. In subsequent cycles, a new reduction peak appears around 0.1 V, related to the lithiation of amorphous silicon, and an oxidation peak near 0.53 V, corresponding to the delithiation process of lithium-silicon alloy.[17] In contrast, the SiCNO HT electrode did not exhibit any noticeable reduction or oxidation peaks in the CV curve, and the corresponding current values were quite low. This observation suggests that the SiCNO HT electrode material exhibits relatively poor lithium storage performance. The differences in the electrochemical behavior between the two materials highlight the superior lithium-ion storage capabilities of the SiCNO MPs compared to the SiCNO

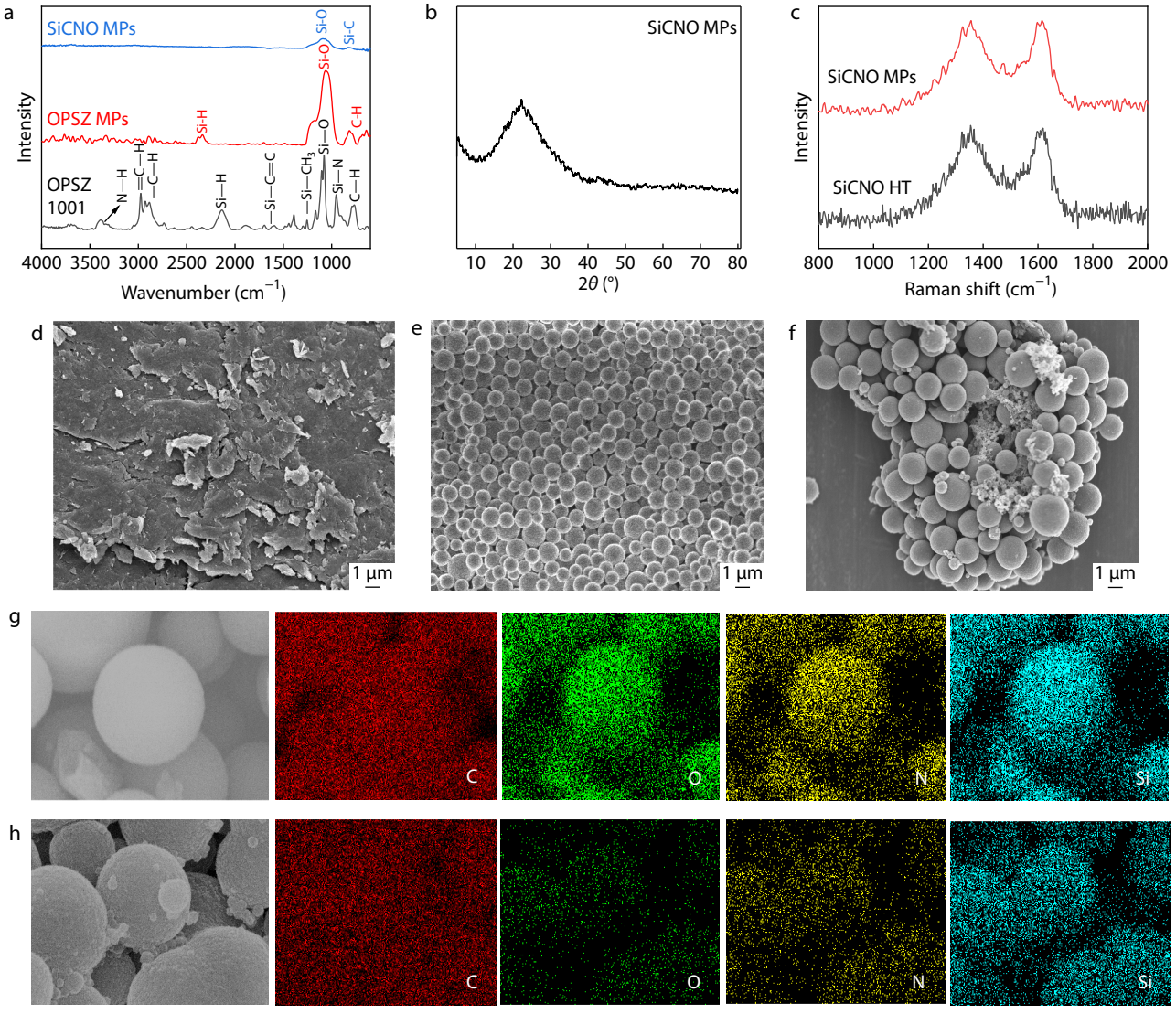

Fig. 2 (a) FTIR spectra of OPSZ 1001, OPSZ MPs and SiCNO MPs; (b) XRD spectra of SiCNO MPs; (c) Raman scattering images of SiCNO MPs and SiCNO; SEM images of (d) OPSZ HT, (e) OPSZ MPs, (f) SiCNO MPs; (g) SEM image and corresponding EDS spectra of C, O, N and Si in OPSZ MPs; (h) SEM image and corresponding EDS spectra of C, O, N and Si in SiCNO MPs.

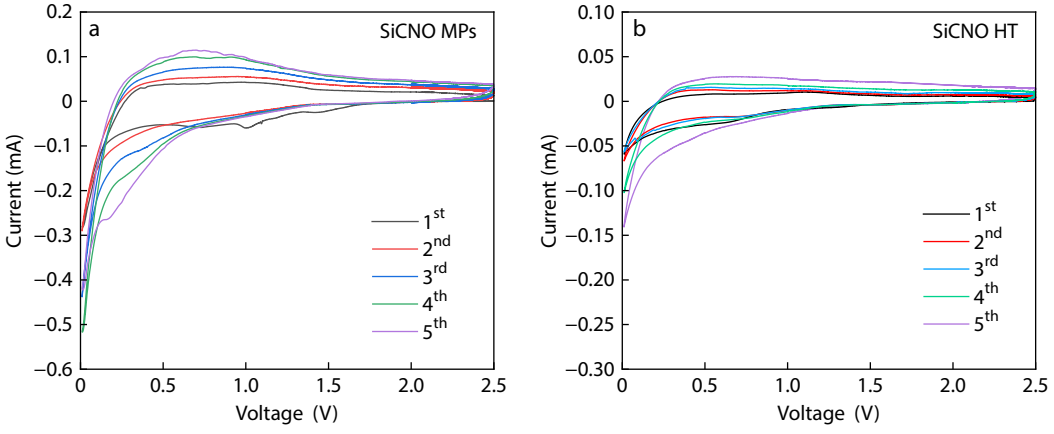

Fig. 3 Cyclic voltammetry curves of (a) SiCNO MPs and (b) SiCNO HT.

https://doi.org/10.1007/s10118-026-3659-9

HT electrode.

The electrochemical charge/discharge behavior of the SiCNO ceramics at a current density of 100 mA·g^{-1} is illustrated by the curves in Fig. 4(a). The initial cycle revealed discharge and charge capacities of 1663.3 and 1123.0 mAh·g^{-1} for SiCNO MPs, corresponding to a first-cycle Coulombic efficiency (CE) of 67.5%. Compared to SiCNO MPs, SiCNO HT exhibited a higher initial discharge capacity (1824.7 mAh·g^{-1}) yet a significantly lower charge capacity (910.1 mAh·g^{-1}), which was reflected in its much lower first-cycle CE of 49.9%. The reason for the low initial coulombic efficiency of these two materials is that the SEI film is formed on the electrode surface during the first charge (lithium intercalation) process, which consumes lithium ions and solvents/salts in the electrolyte, thereby reducing ICE. Second, SiCNO has a high specific surface area, which is conducive to ion transport; however, it also increases the contact area between the electrode and the electrolyte, aggravates the overgrowth and side reactions of the SEI film, and reduces the ICE. Third, SiCNO materials are often amorphous, and their disordered structure may lead to irregular lithium ion insertion/extraction paths. Some lithium ions are 'captured' and are difficult to extract inside the material, resulting in irreversible capacity loss. Compared with the irregular bulk SiCNO HT, the spherical and monodisperse microspheres had a more uniform surface chemical state and fewer defect sites. This helps form a more uniform, possibly thinner, and more stable SEI film, thereby reducing the irreversible lithium consumption caused by SEI overgrowth and uneven rupture/reconstruction during the first cycle.[18]

The charge/discharge cycling performances of the SiCNO MPs and SiCNO HT electrodes at a current density of 100 mA·g^{-1} are shown in Fig. 4(b). The SiCNO MPs electrodes demonstrated excellent electrochemical performance, exhibiting a relatively high specific capacity and coulombic efficiency during charge/discharge cycles. Specifically, after 100 cycles, the SiCNO MPs maintained a discharge-specific capacity of 633.9 mAh·g^{-1} with a high CE of 99.6%. In contrast, the SiCNO HT electrode showed a lower cycling performance, with a discharge-specific capacity of only 449.6 mAh·g^{-1}. The superior cycling performance of the SiCNO MPs electrode can be attributed to its spherical structure, which allows for uniform stress distribution during volume expansion. The rate performance and corresponding Coulombic efficiency of the composites containing SiCNO MPs and SiCNO HT measured at various current densities are illustrated in Fig. 4(c). When the current density was restored to 100 mA·g^{-1} in cycles 31 to

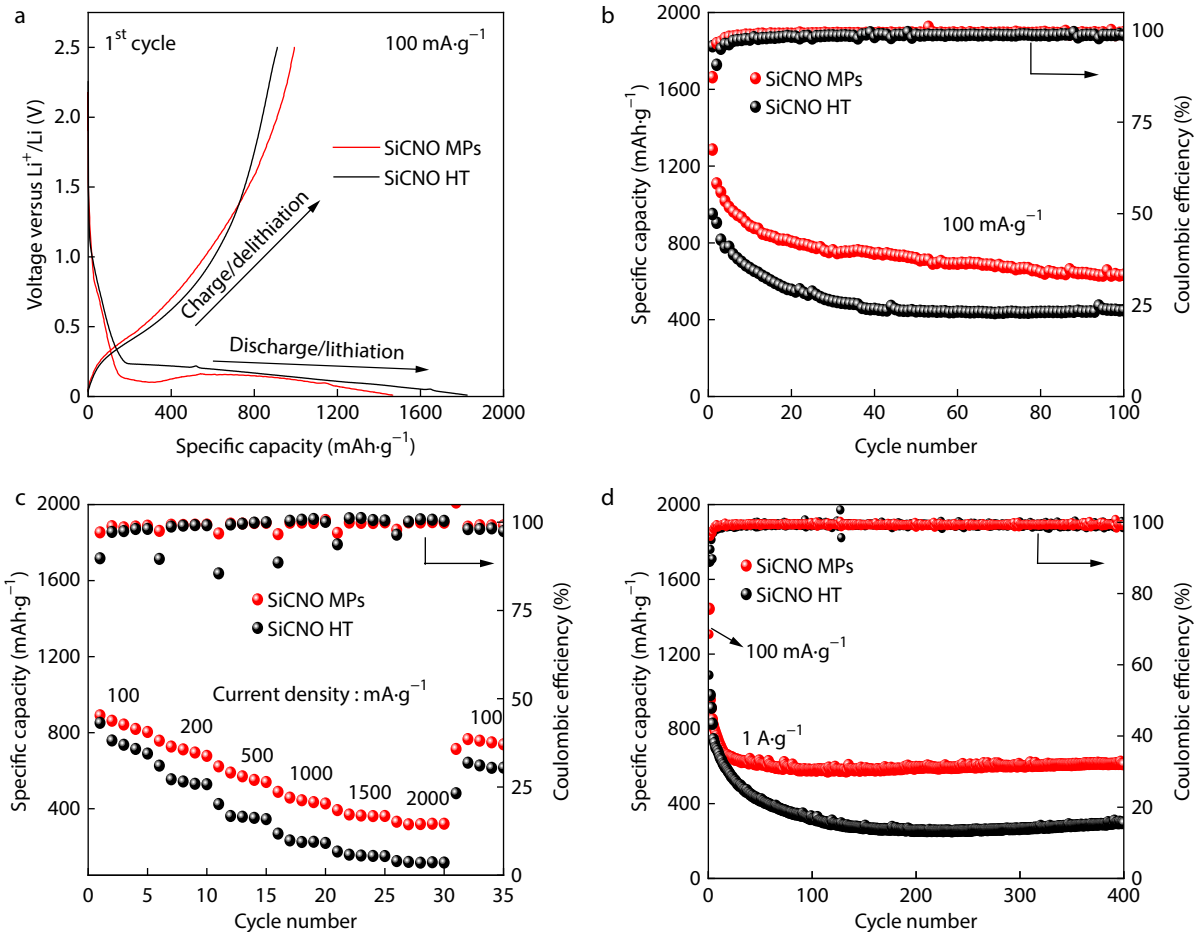

Fig. 4 (a) First cycle voltage profiles of SiCNO MPs and SiCNO HT; (b) Cycling performance and coulombic efficiency of SiCNO MPs and SiCNO HT at a current density of 100 mA·g^{-1}; (c) Rate performance of SiCNO MPs and SiCNO HT; (d) Long-cycle performance of SiCNO MPs and SiCNO HTs at a current density of 1 A·g^{-1}.

https://doi.org/10.1007/s10118-026-3659-9

35, the charge capacity of all electrodes returned to approximately the same level as in Cycle 5. This recovery suggests that the samples retain their structural integrity even under high-rate lithiation/delithiation, with no significant damage. By contrast, the capacity of the SiCNO HTs remained below 200 mAh·g^{-1} at current densities above 1500 mAh·g^{-1}. This difference indicates that the spherical SiCNO microspheres exhibit superior rate performance and stability.

Fig. 4(d) shows the long-term performance of the SiCNO MPs and SiCNO HT electrodes. The electrodes were initially activated for three cycles at 100 mA·g^{-1}. Subsequently, their long-term cycling stability was evaluated over 400 symmetrical discharge/charge cycles at a high current density of 1 A·g^{-1}. The capacity of the SiCNO MPs after 400 cycles is 622.9 mAh·g^{-1}. Although both the SiCNO MPs and SiCNO HT showed good cycling stability and Coulombic efficiency, the initial specific capacity and Coulombic efficiency of the SiCNO MPs electrodes were significantly higher than those of the SiCNO HT electrode. During the entire long-term test, the SiCNO MPs maintained a coulombic efficiency of approximately 98% and demonstrated excellent cycling stability. This high efficiency indicates that only a slight structural degradation occurred over 400 cycles. Compared with other anode materials (Table S2 in ESI), the SiCNO NPs exhibited a superior cycling performance at high current densities. This was attributed to the structural stability caused by the optimal carbon content.

Fig. 5(a) shows the electrochemical impedance spectra (EIS) of the SiCNO MPs and SiCNO HT before the charge and discharge cycles. The specific values of the curves before and after cycling were fitted to further compare the reaction kinetic parameters of the two samples, as detailed in Table S1 (in ESI). The fitting circuit diagram is shown in Fig. 5(b). Figs. 5(c) and 5(d) indicate a decrease in the charge transfer resistance (R_{ct}) after cycling compared with uncycled batteries. This reduction in R_{ct} can be attributed to activation of the negative electrode material.[19] R_{ct} remained relatively unchanged during the subsequent 50 cycles but increased after 100 cycles. However, the SiCNO MPs exhibited a lower charge transfer impedance than the SiCNO HT electrode material. This can be explained by the regular spherical structure of the microspheres, which facilitates charge transfer by providing a short charge-diffusion path within the material. In contrast, the bulk structure of the SiCNO HT is irregular in shape, with poor dimensional uniformity, resulting in a longer diffusion path, lower conductivity, and therefore higher impedance.

To elucidate the lithium storage mechanism of the SiCNO MPs anode, CV measurements were performed at scan rates ranging from 0.1 mV·s^{-1} to 1.0 mV·s^{-1} (Fig. 6a). The CV profiles retained similar shapes across all scan rates, whereas the peak currents increased proportionally with sweep rate. This behavior was quantified by the power-law relationship between the peak current (i) and sweep rate (v).

$$i = av^b \quad (1)$$

where a is a tunable value, and b can be derived from the fitted slope of the lg(v)–lg(i) plot. The b-value indicates the kinetics of charge storage and reveals the corresponding electrode storage mechanism.[20] As depicted in Fig. 6(b), for the cathode/an-

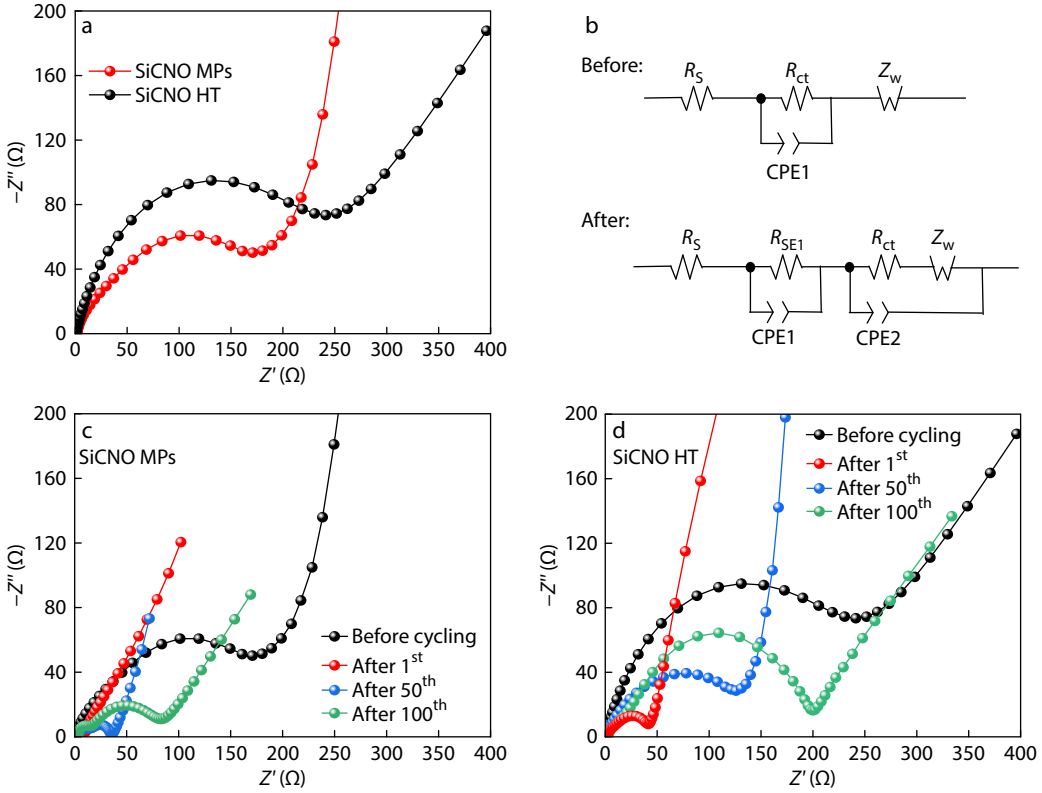

Fig. 5 (a) Nyquist diagram of SiCNO MPs and SiCNO HT electrode before cycling; (b) Equivalent circuit diagram before and after cycling; Nyquist plots of (c) SiCNO MPs and (d) SiCNO HT electrodes before and after cycling.

https://doi.org/10.1007/s10118-026-3659-9

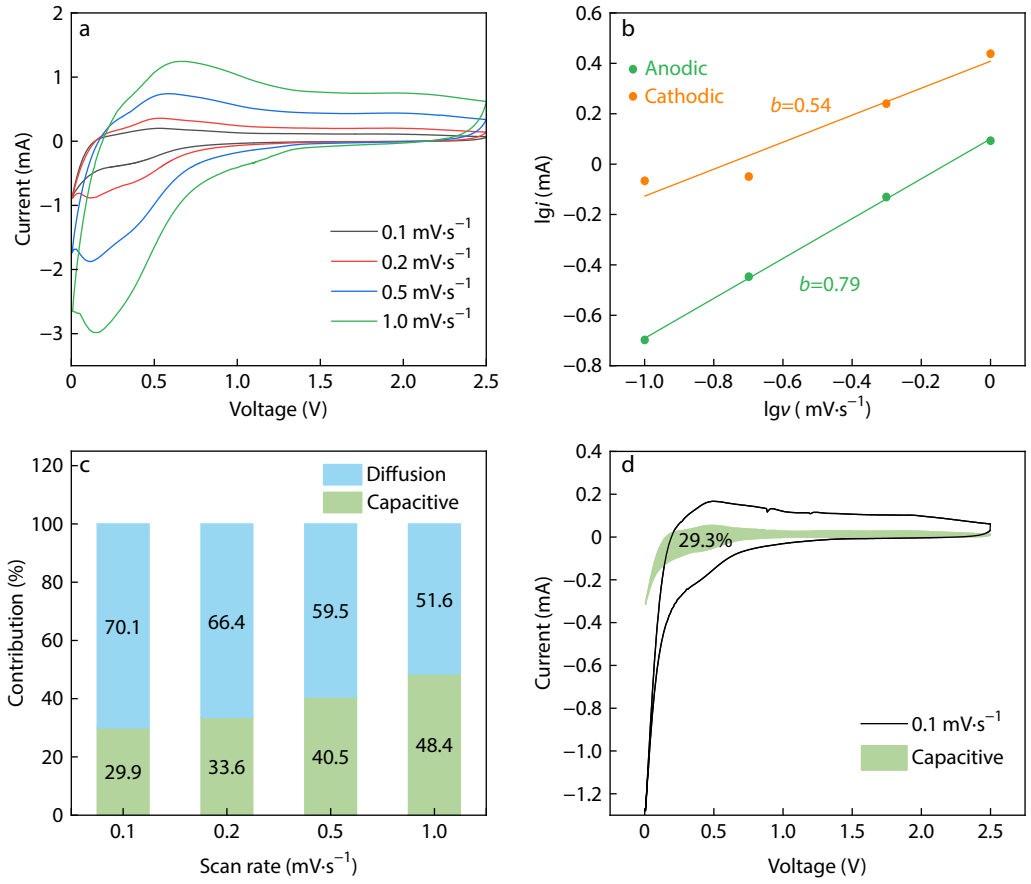

Fig. 6 Electrochemical kinetic analysis of SiCNO MPs composites: (a) CV curves at different scan rates from 0.2 mV·s^{-1} to 1.0 mV·s^{-1}; (b) Relationship between the lg (peak current) and lg (scan rate); (c) Contributions of capacitive charge storage and diffusion-controlled charge storage at different scan rates; (d) Contributions of capacitive charge storage to the total capacity at scan rate 1.0 mV·s^{-1}.

ode peaks, the calculated *b*-value was 0.54/0.79, suggesting that the total capacity consisted of both capacitive and diffusion-controlled processes simultaneously. Furthermore, at a given scan rate (v), the total measured current (i) originated from two distinct contributions: a surface-dominated pseudocapacitive process (k_1v) and a bulk diffusion-controlled process ($k_2v^{1/2}$). This can be expressed quantitatively by the following relationship:

$$i(v) = k_1v + k_2v^{1/2} \quad (2)$$

The increase in the pseudocapacitance contribution with increasing scan rate and the corresponding decrease in the diffusion contribution indicate that the pseudocapacitance control process has a significant impact on the total electrode capacity, especially at higher scan rates (Fig. 6c). In addition, it is possible to calculate the k_1 and k_2 values, allowing for the distinction between the percentage contributions of the capacitance-controlled and diffusion-controlled mechanisms. According to the analysis, the surface pseudo capacitance contribution of SiCNO MPs electrodes at 0.1 mV·s^{-1} is about 29.3% (Fig. 6d).

SEM was used to examine the morphology of the two electrodes after 100 lithiation/delithiation cycles to further evaluate the structural stability of the SiCNO HT and MP composites. The SEM images reveal significant differences between the two materials. After 100 charge/discharge cycles, the SiCNO MPs electrodes maintained their structural integrity, as evidenced by the relatively smooth and flat surface that was free of significant cracks or degradation. (Figs. 7a and 7b). This suggests that the structural integrity of the material was preserved during cycling. In contrast, the SiCNO HT electrodes exhibited significant morphological changes after 100 charge/discharge cycles. The surface became rough, exhibiting visible delamination and cracking (Figs. 7c and 7d, respectively). These changes suggest that the material underwent structural degradation during cycling. This reflects the change in volume expansion before and after the cycle. The volume expansion rate can be approximated as the rate of increase in the thickness. This can be expressed quantitatively by the following relationship:

$$\text{Volume expension rate (\%)} = \frac{V_f - V_i}{V_i} \times 100\% \approx \frac{t_f - t_i}{t_i} \times 100\% \quad (3)$$

where V_i and V_f represent the volume of the electrode before and after 100 cycles, respectively, and t_i and t_f denote the thicknesses of the electrode before and after 100 cycles, respectively. The thickness increased substantially for both materials: SiCNO MPs grew from 26.5 μm to 49.2 μm, and SiCNO HT from 25.8 μm to 53.1 μm, with the latter exhibiting a more pronounced increase. (Figs. 7e–7h). The smaller increase in thickness and better structural retention in the SiCNO MPs are attributed to the higher dispersion of spherical particles in the electrode material, ensuring full contact with the conductive substrate. This im-

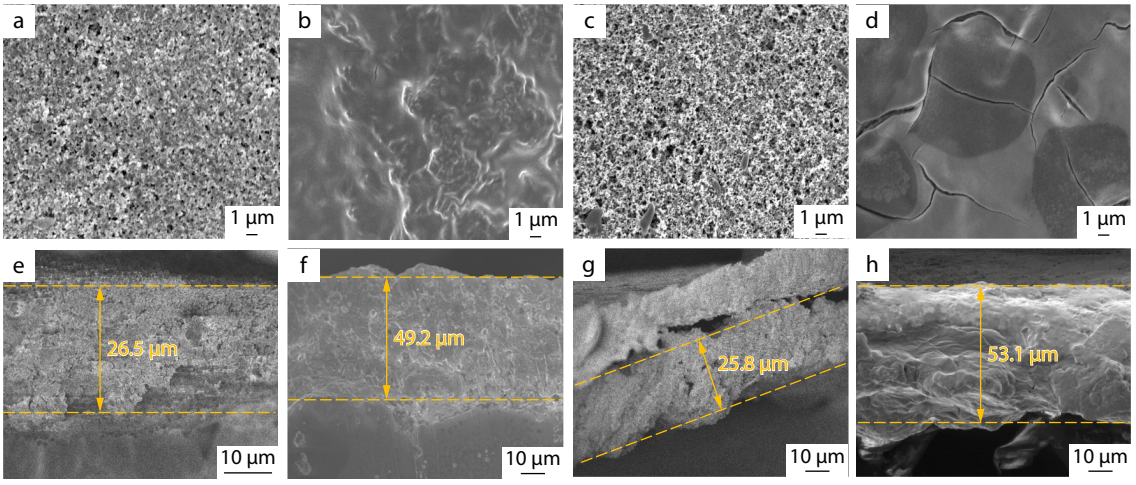

Fig. 7 SEM images of SiCNO MPs electrode (a, b) and SiCNO HT electrode (c, d) before and after 100 charge-discharge cycles. Corresponding cross-sectional SEM images of the SiCNO MPs electrode (e, f) and SiCNO HT electrode (g, h) before and after 100 charge-discharge cycles.

proved the electrical connectivity and mitigated the volume expansion stress in the entire electrode. The spherical geometry of the SiCNO MPs provided isotropy, allowing for uniform volume changes in all directions during cycling. This isotropy allows for uniform volume changes in all the directions during cycling. This isotropy reduces the likelihood of comminution and fragmentation, contributing to the material-enhanced cycling stability compared with the irregularly shaped SiCNO HT.[21] This analysis underscores the superior structural stability of SiCNO MPs over SiCNO, making it a more reliable material for long-term lithium-ion battery applications.

To further explore the lithium-ion storage mechanism of the SiCNO materials, XPS characterization was performed on the electrode materials in different charging and discharging states, as shown in Fig. S8 (in ESI). The XPS spectra of Si 2p showed that during discharge to 0.01 V, the binding energy of Si 2p shifted to a lower value. Upon charged to 2.5 V, the binding energy shifted back to a higher position. This shift indicates a redox reaction between the SiCNO and Li ions during the cycling process. When discharged to 0.01 V, there are three peaks of Si—O—Si bonding around 101.2 eV, Si—Si/Si—O—Li bonding (about 100.6 eV, and Li—Si bonding (about 99.9 eV).[22] At charging to 2.5 V, it can be seen that the peak strength of the Li—Si bond is greatly reduced, but the peak strength of the Si—Si bond is significantly increased, indicating that most of the Li_xSi is converted back to Si during the delithiation process, with some irreversible products such as Li_4SiO_4 remaining.[23] The peak strength of the Si—O—Si bond is approximately 100.6 eV and that of the Si—Si/Si—O—Li bond is approximately 99.9 eV. The presence of a small number of Li—Si bonds even after charging to 2.5 V suggests incomplete delithiation, which may contribute to capacity loss over cycles.[24]

CONCLUSIONS

In this study, organopolysilazane microspheres (OPSZ MPs) were synthesized *via* the free radical polymerization of silazane oligomers initiated by azobisisobutyronitrile (AIBN). By varying the reaction conditions, such as the concentration of the silazane oligomer, amount of initiator content, reaction temperature, and reaction time, the particle size and distribution of the microspheres were controlled, resulting in well-dispersed OPSZ MPs. These OPSZ MPs were then pyrolyzed at high temperatures to form SiCNO ceramic microspheres (SiCNO MPs), which were used as active materials for anodes in lithium-ion batteries. Compared to SiCNO HT (prepared by high-temperature curing), SiCNO MPs have a regular spherical structure with a large specific surface area, which can shorten the ion/electron transport paths and upgrade their cycling and multiplicity performance. The spherical structure also helped in the better dispersion of stress from volume expansion, thus suppressing the extent of expansion. Therefore, the SiCNO microspheres exhibited an initial discharge-specific capacity of 1663.3 $mAh·g^{-1}$. After 100 charge/discharge cycles at a current density of 100 $mAh·g^{-1}$, the MPs retained a capacity of 633.9 $mAh·g^{-1}$. Even after 400 cycles at a high multiplication rate of 1 $A·g^{-1}$, the reversible capacity remained at 622.9 $mAh·g^{-1}$. The SiCNO MPs exhibited superior structural stability during lithiation/delithiation, with a volume expansion of 85.66% during cycling.

Conflict of Interests

The authors declare no interest conflict.

Electronic Supplementary Information

Electronic supplementary information (ESI) is available free of charge in the online version of this article at http://doi.org/10.1007/s10118-026-3659-9.

Data Availability Statement

The data that support the findings of this study are available from the corresponding author upon reasonable request.

ACKNOWLEDGMENTS

This study was financiallly supported by the International

Science and Technology Assistance Program of the Ministry of Science and Technology (No. KY202001016), Shandong Provincial Natural Science Foundation Magnitude Fundamental Research, China (No. ZR2022ZD11), Qingdao New Energy Shandong Laboratory Open Project (No. QNESL OP202312), the Doctoral Fund of Qingdao University of Science and Technology (No. 12030430010828), the Shandong Provincial Natural Science Foundation (No. ZR2020QB026), the Shandong Natural Science Excellent Youth Fund (No. ZR2019YQ22), and the Introduction and Cultivation Plan of Young Innovative Talents in Colleges and Universities of Shandong Province (2019).

REFERENCES

1 Ren, W.; Zhou, Y.; Li, J.; Huang, L.; Sun, S. Si anode for next-generation lithium-ion battery. *Curr. Opin. Electrochem.* **2019**, *18*, 46–54.
2 Xu, Q.; Li, J.; Sun, J.; Yin, Y.; Wan, L.; Guo, Y. Watermelon-inspired Si/C microspheres with hierarchical buffer structures for densely compacted lithium-ion battery anodes. *Adv. Energy Mater.* **2017**, *7*, 1601481.
3 Zhang, Y.; Huang, H.; Chen, X.; Gao, T.; Li, J.; Yao, Y.; Xu, Z.; Zheng, M.; Liu, Z. Facile synthesis of graphite-SiO_x/C core-shell composite anode for high stable lithium-ion batteries. *Energy Fuels* **2024**, *38*, 23140–23149.
4 Mera, G.; Navrotsky, A.; Sen, S.; Kleebe, H.; Riedel, R. Polymer-derived SiCN and SiOC ceramics - structure and energetics at the nanoscale. *J. Mater. Chem. A* **2013**, *1*, 3826–3836.
5 Jiang, J.; Zhang, Y.; Guo, X.; Zhang, H. Narrow or monodisperse, highly cross-linked, and "living" polymer microspheres by atom transfer radical precipitation polymerization. *Macromolecules* **2011**, *44*, 5893–5904.
6 Zhang, B.; Lu, J.; Liu, X.; Jin, H.; He, G.; Guo, X. Synthesis of controllable carboxylated polystyrene microspheres by two-step dispersion polymerization with hydrocarbon alcohols. *Int. J. Polym. Sci.* **2018**, *2018*, 702597.
7 Zhang, Z.; Calderon, J.; Fahad, S.; Ju, L.; Antony, D.; Yang, Y.;

Graphical Abstract

Micro-sized Silicon Carbonitride Prepared by Radical Polymerization as a High-performance Anode Material for Lithium-ion Batteries

Xin Xia, Zhen-Peng Zhang, De-Shuo Wang, Yi-Han Li, Jing-Jiang Sun, Jian-Jiang He, Qing-Fu Wang, and Wei Zhao

Qingdao University of Science and Technology

Organopolysilazane oligomers undergo free radical polymerization to produce uniform polymer microspheres, which are then pyrolyzed at about 1000 °C in N_2 to form amorphous SiCNO ceramic microspheres with embedded free carbon domains. This unique structure enables the material to achieve high capacity, excellent long-term cycling stability, and robust structural integrity as a lithium-ion battery anode.

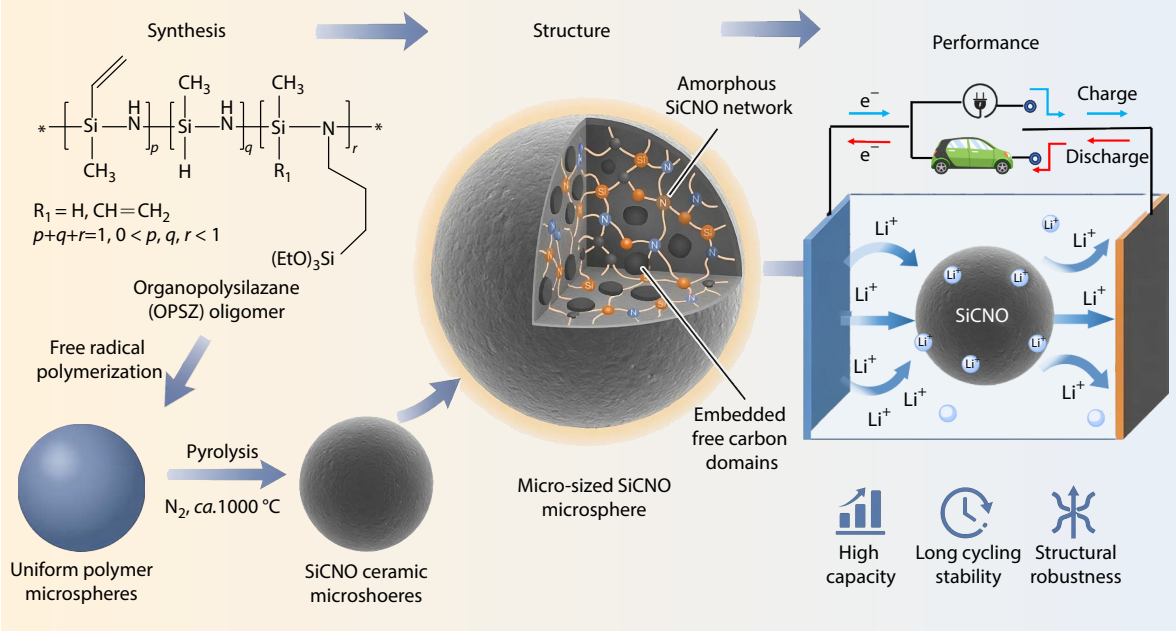

Chinese J. Polym. Sci. 2026, 44, 2659–2669 *https://doi.org/10.1007/s10118-026-3659-9*

Kushima, A.; Zhai, L. Polymer-derived ceramic nanoparticle/edge-functionalized graphene oxide composites for lithium-ion storage. *ACS Appl. Mater. Interfaces* **2021**, *13*, 9794–9803.
8 Gao, B.; Li, D.; Lei, Q. Preparation of high PMMA grafted particle SiO_2 using surface initiated free radical polymerization. *J. Polym. Res.* **2011**, *18*, 1519–1526.
9 Ionescu, E.; Kleebe, H.; Riedel, R. Silicon-containing polymer-derived ceramic nanocomposites (PDC-NCs): preparative approaches and properties. *Chem. Soc. Rev.* **2012**, *41*, 5032–5052.
10 Esteves, A.; Brokken-Zijp, J.; Laven, J.; Huinink, H.; Reuvers, N.; Van, M.; de With, G. Influence of cross-linker concentration on the cross-linking of PDMS and the network structures formed. *Polymer* **2009**, *50*, 3955–3966.
11 Chavez, R.; Ionescu, E.; Balan, C.; Fasel, C.; Riedel, R. Effect of ambient atmosphere on crosslinking of polysilazanes. *J. Appl. Polym. Sci.* **2011**, *119*, 794–802.
12 Liu, Y.; Lin, X.; Gong, H.; Zhang, Y.; Feng, Y.; Mao, J.; Xie, B. Electromagnetic properties and microwave absorption performances of nickel-doped SiCN ceramics pyrolyzed at different temperatures. *J. Alloys Compd.* **2019**, *771*, 356–363.
13 Chen, J.; Mao, Z.; Zhang, L.; Wang, D.; Xu, R.; Bie, L.; Fahlman, B. Nitrogen-deficient graphitic carbon nitride with enhanced performance for lithium-ion battery anodes. *ACS Nano* **2017**, *11*, 12650–12657.
14 Ying, H.; Yang, T.; Zhang, S.; Guo, R.; Wang, J.; Han, W. Dual immobilization of SnOx nanoparticles by N-doped carbon and TiO_2 for high-performance lithium-ion battery anodes. *ACS Appl. Mater. Interfaces* **2020**, *12*, 55820–55829.
15 Guo, X.; Li, W.; Geng, P.; Zhang, Q.; Pang, H.; Xu, Q. Construction of SiOx/nitrogen-doped carbon superstructures derived from rice husks for boosted lithium storage. *J. Colloid Interface Sci.* **2022**, *606*, 784–792.
16 Feng, Y.; Wei, Y.; Jia, Z.; Zhang, Y.; Battaglia, V.; Liu, G. Polymer-derived and sodium hydroxide-treated silicon carbonitride material as anodes for high electrochemical performance Li-ion batteries. *ChemistrySelect* **2016**, *1*, 309–317.
17 Xu, B.; Shen, H.; Ge, J.; Tang, Q. Improved cycling performance of $SiOx/MgO/Mg_2SiO_4$/C composite anode materials for lithium-ion battery. *Appl. Surf. Sci.* **2021**, *546*, 148814.
18 Shi, H.; Yuan, A.; Xu, J. Tailored synthesis of monodispersed nano/submicron porous silicon oxycarbide (SiOC) spheres with improved Li-storage performance as an anode material for Li-ion batteries. *J. Power Sources* **2017**, *364*, 288–298.
19 Yin, L.; Park, M.; Jeon, I.; Hwang, J.; Kim, J.; Lee, H.; Park, M.; Jeong, S.; Cho, C. Silicon nanoparticle self-incorporated in hollow nitrogen-doped carbon microspheres for lithium-ion battery anodes. *Electrochim. Acta* **2021**, *368*, 137630.
20 Xiao, Z.; Lei, C.; Yu, C.; Chen, X.; Zhu, Z.; Jiang, H.; Wei, F. $Si@Si_3N_4$@C composite with egg-like structure as high-performance anode material for lithium ion batteries. *Energy Storage Mater.* **2020**, *24*, 565–573.
21 Zhang, L.; Al-Mamun, M.; Wang, L.; Dou, Y.; Qu, L.; Dou, S.; Liu, H.; Zhao, H. The typical structural evolution of silicon anode. *Cell Rep. Phys. Sci.* **2022**, *3*, 100811.
22 Takezawa, H.; Iwamoto, K.; Ito, S.; Yoshizawa, H. Electrochemical behaviors of nonstoichiometric silicon suboxides (SiO_x) film prepared by reactive evaporation for lithium rechargeable batteries. *J. Power Sources* **2013**, *244*, 149–157.
23 Philippe, B.; Dedryvère, R.; Allouche, J.; Lindgren, F.; Gorgoi, M.; Rensmo, H.; Gonbeau, D.; Edström, K. Nanosilicon Electrodes for lithium-ion batteries:interfacial mechanisms studied by hard and soft X-ray photoelectron spectroscopy. *Chem. Mater.* **2012**, *24*, 1107–1115.
24 Han, M.; Mu, Y.; Yuan, F.; Liang, J.; Jiang, T.; Bai, X.; Yu, J. Vertical graphene growth on uniformly dispersed sub-nanoscale SiO_x/N-doped carbon composite microspheres with a 3D conductive network and an ultra-low volume deformation for fast and stable lithium-ion storage. *J. Mater. Chem. A* **2020**, *8*, 3822–3833.

https://doi.org/10.1007/s10118-026-3659-9